AN ELECTROMAGNETIC HEAD AND NECK HYPERTHERMIA APPLICATOR: EXPERIMENTAL PHANTOM VERIFICATION AND FDTD MODEL

Margarethus M. Paulides, M.Sc., Jurriaan F. Bakker, B.Sc.
and Gerard C. van Rhoon, Ph.D.

Erasmus MC - Daniel den Hoed Cancer Center,
Department of Radiation Oncology, Section Hyperthermia
PO box 5201, NL-3008 AE, Rotterdam, The Netherlands
Tel.no. : +31 10 4391676
Fax.no. : +31 10 4391022
E-mail: M.Paulides@ErasmusMC.nl

August 22, 2007

Running title: "H&N applicator prototype: verification and model"

Abstract

Purpose: Experimental verification of the feasibility of focussed heating in the neck region by an array of two rings of six electromagnetic antennas. We further measured the dynamic specific absorption rate (SAR) steering possibilities of this setup and compared these SAR patterns to simulations.
Methods and Materials: By a specially constructed laboratory prototype head and neck applicator, including a neck mimicking cylindrical muscle phantom, we performed SAR measurements by electric-field Schottky-diode sheet measurements and, using the power-pulse technique, by fiberoptic thermometry and infra-red (IR) thermography. Using phase-steering, we also steered the SAR distribution in radial and axial directions. All measured distributions where compared to predictions by a finite-difference time-domain (FDTD)-based electromagnetic simulator.
Results: A central 50% iso-SAR focus of 35mm (±3mm) in diameter and around 100mm (±15mm) in length are obtained for all investigated settings. Further, this SAR focus can be steered towards the desired location in radial and axial direction with an accuracy of ∼5mm. SAR distributions as measured by all three experimental methods are well predicted by the simulations.
Conclusions: We conclude that focussed heating in the neck is feasible and that this focus can effectively be steered in both radial and axial direction. For quality assurance (QA) measurements we conclude that the Schottky-diode sheet provides the best compromise between effort, speed and accuracy, though a more specific and improved design is warranted.

Key words: Hyperthermia, SAR, measurements, antenna array, head and neck tumours.

1 Introduction

Loco-regional control of advanced carcinomas in the head and neck (H&N) region still poses a major therapeutic challenge [1] [2] and treatment related toxicity remains a major issue in this region [3]. Combining hyperthermia (HT) to the current treatment modalities has a high potential to increase treatment outcome without increasing toxicity [4]. Recent phase III trials have shown the benefit of the addition of HT to current treatment modalities for various tumour sites [5], [6], [7]. Valdagni *et al.* [8] [9] have demonstrated that with a non-site-specific HT-applicator already a significant increase in local control (from 24% for radiotherapy (RT) alone versus 69% for RT plus HT) is achieved for metastatic lymphnodes in stage IV carcinoma of the H&N. Extension of the hyperthermia application to deeper located tumours is cumbersome with the available applicators and therefore requires a specific designed applicator that is also expected to contribute to a better treatment quality for this site [10] [11].

In recent years, we have investigated the ability of a multi-element circumferential

H&N HT applicator to deposit radiofrequency (RF) energy selectively in the center of the neck [12]. Optimum frequencies were shown to be in the frequency band between 300 and 600MHz for all realistic target sizes therefore we selected 433MHz[1] as operating frequency. Further, we found that eight antenna elements provide sufficient focussing for selective heating. Building on these findings, we analyzed the influences of the anatomy on the SAR pattern [13]. In this study we found that muscle phantom measurements are predictive for SAR pattern in the middle of the neck. Due to the spine, the central SAR focus changes from a circular to a more donut shape but the central focus remains at its central position. Subsequently, research was conducted into possibilities of further improving the power absorption pattern by going from one to two or three antenna rings [14], which provides also axial steering possibilities. We established that heating at depth is highly correlated with the amount of antennas arranged in multiple rings. Multiple rings enable steering in the direction of the patient axis which is well validated for deep hyperthermia [15] [16] but needs confirmation for the head and neck application. This work resulted in a final setup design: a setup with two rings of six antennas each operating at 433MHz. As radiators, we selected a patch antenna setup that is simple, low-cost, efficient and small and we designed it specific for the head and neck applicator [17]. Another major advantage of this antenna design is that no matching network is required, which facilitates a better control of the input parameters of the setup and hence provides better possibilities to create a representative model. Subsequently, the latter improves the reliability and accuracy of numerical predictions.

Aim of the present study was to experimentally verify the feasibility of focussed heating in the head and neck region using an array of two rings of six antennas by the split-phantom technique. Simultaneously, we established the accuracy of the predictions of our electromagnetic simulation model. Finally, we explored the dynamic SAR steering behavior of the antenna array. Hereto we constructed a laboratory prototype applicator consisting of twelve patch antenna elements and a muscle-equivalent neck phantom. We performed measurements with this setup and compared them to predicted SAR patterns.

2 Methods and materials

2.1 Prototype design

Figure 1 shows a picture of the bottom half of the prototype applicator and Figure 2 visualizes an exploded view of it's two parts. These parts can be separated to allow 2D IR measurements or positioning of measurement devices: glass fiber probes or electric (E)-field Schottky-diode sheet. Both parts of the applicator consist of a semi-circular PVC backplane (diameter = 30cm, length = 60cm: Figure 3) and PVC shields at both ends.

[1] 433MHz is an ISM frequency: a frequency available for Industry Science and Medicine

Both half backplanes are covered, waterproof, with a 50μm thick ABS copolymer sheet that is glued on a frame that can be mounted on the backplanes (see Figure 2). Twelve antenna elements are mounted on the PVC backplanes in a 2x6 arrangement [14], i.e. two rings (distance = 8cm, ring-radius = 30cm: see Figure 3) of six equidistantly spaced patch antennas. We defined the origin of the applicator between the rings so the antennas in these rings are located at z = -4cm and z = 4cm. The water in the prototype was circulated and temperature controlled by two E4850 refrigerated recirculators (Bio-Rad, Microscience Division).

Every patch antenna [17] consists of a, resonant, 2mm-thick brass patch (width = 12mm, length = 25mm) that is asymmetrically (the distance from the rod to the side of the patch is 0.5mm) mounted on the extending conducting rod of a C-female receptacle connector. Coaxial cables are used to transfer the 433.92MHz signal from PG70.150.2 power generators (SSB Electronic, Germany) to the applicator. The conducting backplane required for the patch antenna design is formed by soft copper tape (thickness: 35μm + 25μm adhesive) that covers the inner side of both PVC backplanes (see Figure 1).

Two PVC semi-cylinders (muscle cylinder diameter = 11.6cm, PVC thickness = 1.5mm) [2] filled with muscle equivalent material, representing the neck of a patient, are positioned at the center of the prototype. The muscle-equivalent material was created using a recipe described by Ito *et al.* [18] and had properties in accordance with Gabriel *et al.* [19] (see Table 1).

2.2 EM modelling

We predicted the SAR distributions in the prototype applicator using SEMCAD [20]. SEMCAD has a FDTD kernel that can be used for dosimetric simulations. It includes a solid modeling kernel in which we created a full 3-D model using the exact dimensions of the applicator prototype and muscle phantom. The very thin sheets between the semi-cylinders were neglected for calculations. Further, in stead of modeling the complete connector and the transmission line, we used the commonly accepted approach to apply a voltage source at the gap between the conducting backplane and the rod of the patch antenna [21], which provides accurate field distributions [22]. This solid model was converted automatically into a grid implementation with maximum gridsteps of $\lambda/15$ and grid refinements at the locations of the antennas ($\lambda/250 < \Delta < \lambda/80$), i.e. a total of $\sim$5Mcells. The grid refinements at the antennas were required to accurately model the (important) small dimensions of the antenna and the non-orthogonally placement in the grid, at the location of the feeding rod. Table 1 shows the properties of all the materials used in the simulation. Properties of demineralized water (salinity = 0.04 g/l, T = 25°C) were found

[2] The dimensions of the phantom approximately equal an average neck [13]

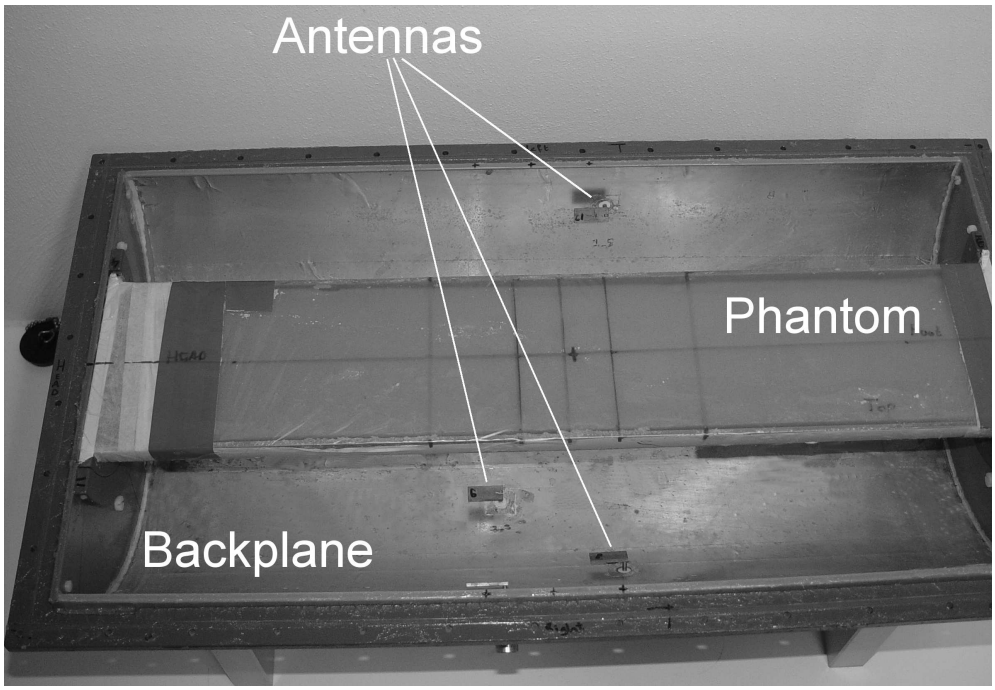

Figure 1: Picture of the bottom half of the prototype with the sheet and its frame excluded. Visible are the copper-tape that covers the backplane, one half of the muscle phantom and multiple patch antennas

in a publication of Stogryn [23]. We exited the voltage sources at all gaps at 433MHz and steady state was obtained after ∼25 periods.

Table 1: Properties of the materials at 433MHz

Material	ρ (kg/m^3)	ϵ_r (-)	σ_{eff} (S/m)
Muscle phantom	900	56	0.8
PVC	1350	2.2	0.004
Demineralized water	1000	78	0.04

2.3 Measurements

Three SAR pattern measurement methods were used because they all have their own features: their major strengths are either accuracy (Fiberoptic thermometry), resolution (IR thermography) or speed (E-field Schottky diode sheet). These measurement methods and their results were compared to establish the optimum method for quality assurance. Waterbolus temperatures where chosen such that mean temperatures in the prototype were around 22°C at which the phantom properties are reported, i.e. the waterbolus temperatures was 18-19°C for the power-pulse measurements (T-probes and IR) and 22°C

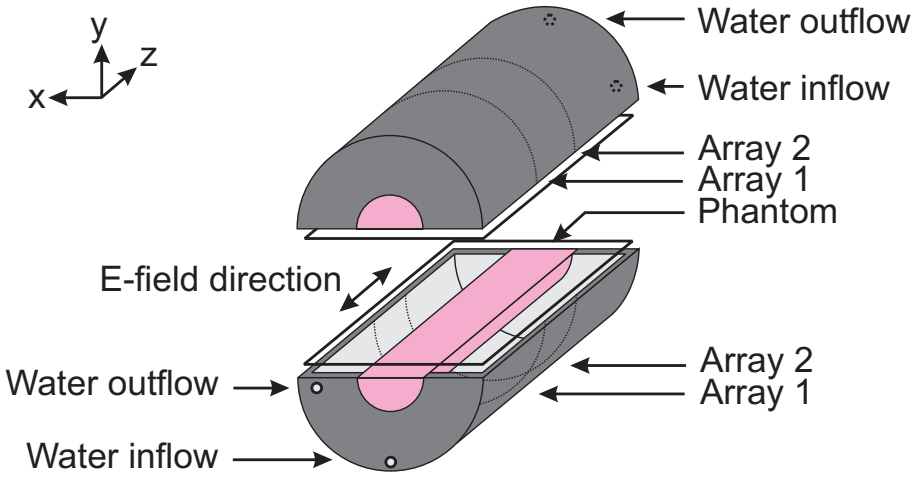

Figure 2: Exploded view of the prototype that is constructed in two parts for measurements (T-probes, E-field sheet, IR pictures). Visible are the phantom semi-cylinders (pink/light grey), the two frames spanning the sheet, the PVC backplanes (dark grey) and the copper tape on the inside of the backplanes (light grey).

for the E-field measurements. Figure 3 shows a cross-section through the applicator at y=0cm and a zoomed version of the SAR distribution obtained by taking IR pictures before and after heating.

2.3.1 Fiberoptic thermometry

Temperatures were measured with 24 Takaoka FTP1 standard sensor probes (accuracy = 0.1°C, precision = 0.1°C), which are read with a Takaoka FT1310 fiber thermometer (Takaoka Electric MFG Co. Ltd., Japan) with a refresh rate of 3s. These non-metallic probes were positioned at the main axes between both halves of the prototype. The local SAR was measured using the power pulse method: the change of temperature (3-10°C) in a phantom is measured while applying a high power (300-600W) for a short time (90-300s) at the antennas of the applicator [24] (see Figure 5). To reduce influences of heat conductivity a short heating time is required, therefore we used a high power to obtain accurately measurable temperature changes. The local SAR is calculated from the temperature rise via:

$$SAR(x, y = 0, z) = c \cdot \frac{\Delta T(x, y = 0, z)}{\Delta t}, \tag{1}$$

where c is the specific heat capacity of the muscle phantom material (3.63 kJ kg^{-1} K^{-1}), ΔT is the local temperature rise [K] and Δt is the corresponding heating time [s]. We assumed no electric field disturbing effect of the fiber probes.

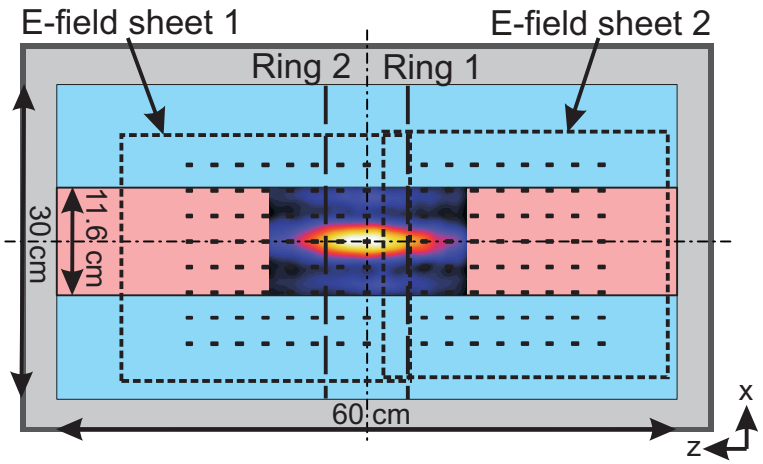

(a)

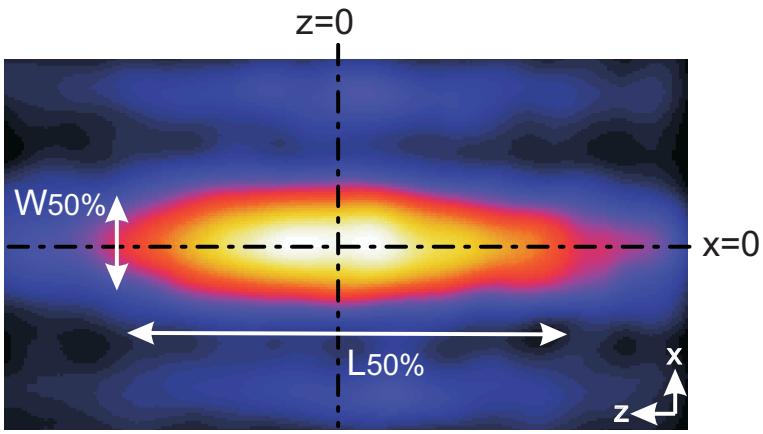

(b)

Figure 3: Cross-section through the prototype at y = 0cm with a SAR distribution obtained from two IR pictures (before and after heating) for central settings (a) and a zoomed version of this SAR distribution (b). In (a), the location of the Schottky diodes (E-field sheet 1 and 2) is indicated by the black rectangles and the extends of the sheets by the dotted lines. Further, the location of the antenna rings and the main dimensions of prototype and phantom are indicated. T-probe measurements are taken at locations on "x=0" and "z=0". In (b) the colorscale is from black (0%) to white (100%) and the length ($L_{50\%}$) and width ($W_{50\%}$) of the focus, i.e. the 50% iso-SAR contour, are indicated.

2.3.2 IR thermography

We used IR thermography to visualize the temperature (rise) pattern at a high resolution (320x236 pixels). Pixel size was determined by taking an IR picture of a hot object with known dimensions: for our setup the dimensions were 0.5x0.5mm^2. After application of power, the top halve was removed and IR pictures were taken using a TVS-600 infrared camera (Nippon Avionics Co. Ltd., Japan) that was mounted on a solid framework. From the IR picture before and after heating we calculated the SAR pattern using equation 1. The inevitable time between end of heating and first IR picture was kept as short as possible (typically $\sim 10s$) in an attempt to reduce influences of heat conductivity.

2.3.3 E-field Schottky-diode sheet

For fast measurements, which also enables studying the prototypes dynamic behavior, we performed SAR measurements also with the E-field Schottky diode sheet, that is described in Kaatee et al. [25] and Van Rhoon et al. [26]. Hereto, two sheets were positioned between both halves of the prototype (Figure 3). To avoid a decrease in sensitivity caused by overlapping sheets at the location of the diodes[27], we used a distance between both sheets such that one row of measurement points was absent. SAR values can be calculated from the amplitude of the measured E-field values, using the effective conductivity (σ_{eff}) and mass-density (ρ), according to:

$$SAR(x, y = 0, z) = \sigma_{eff} \cdot \frac{|E(x, y = 0, z)|^2}{2\rho}. \quad (2)$$

The E-field sheet directly measures real-time the axial (z) component of the E-field. Also, variations in dielectric properties of the phantom materials are much lower because measurements can be performed at low power (120W). Further, no manipulation of the setup is required for multiple measurements, i.e. all distributions can be measured using one single disposition of the experimental setup. Without calibration their accuracy is 6% [26], however when airgaps are present close to the diodes this accuracy is reduced due to lower sensitivity. A main disadvantage of the current design of the sheet is its poor spatial resolution for measurements at 433MHz, i.e. the distance between two diodes is 2.5cm ($\sim \lambda/4$).

2.3.4 Measurement procedures and phase settings

As a first step we measured impedance characteristics of the antennas using an 8751A network analyzer (Agilent Technologies, USA) to verify that they were sufficiently resonant. As a side step we also assessed the amount of cross-coupling using the network analyzer. Fiberoptic and IR measurements were conducted simultaneously. Hereto we positioned an IR camera above the prototype and positioned the probes between both halves of the

prototype. High power was applied and simultaneously we measured temperatures with the fiber probes (see Figure 5). After the required maximum temperature change was obtained we opened the applicator and took IR pictures. After heating we used a cooling time of typically 2 hours between subsequent measurements to obtain a homogeneous thermal distribution. E-field sheet measurements were performed separately at low power to avoid variations in dielectric properties of the phantom due to temperature differences. To check for measurement errors, all measurements were conducted multiple times in a time period of a year and the muscle phantom was newly constructed two times.

To obtain a central focus for each antenna (i) on each ring (j) we used central power (P) and phase (φ) settings ($P_{j,i}$ = 25W and $\varphi_{j,i}$ = 0). Subsequently, we investigated the possibilities of SAR steering in radial and axial direction by using a phase-steering method in analogy to the method that is used in the BSD2000 Sigma-60 system [28] [29]. For each antenna, we analytically calculated the required phase-delays ($\varphi_{i,j}$), using the difference in wave velocity in muscle and water, such that maximum interference occurs at the desired Target Center Point (TCP). For this analytical model we assumed a muscle cylinder (radius is 5.8cm) and two circumferential arrays (radius = 14.15cm) of six point-sources at z = -4cm and z = +4cm and we neglected the PVC phantom-shell.

3 Results

3.1 Reflection and cross-coupling

After one year, reflection coefficients had increased due to degradation (oxidation) of the setup (mainly the copper tape of the groundplane). Figure 4 shows the typical reflection coefficients of all antennas in the array at 23°C and 25°C halfway during our measurement period. This figure clearly shows that the reflection coefficient is influenced by the temperature of the water in the waterbolus. For both temperatures these reflection coefficients are all beneath -10dB (∼6% reflection on average) so efficiency of the antennas was sufficient for the purposes of our measurements. For the clinical applicator, however, we constructed a redesign that has somewhat improved reflection characteristics [17]. For this qualitative analysis we neglected the influences of the variations in efficiency (∼6%) for the antennas of the prototype. We further found low cross-coupling between the antennas: maximum -22dB (0.6%) and on average -27dB (0.2%). The lowest values where obtained for neighboring antennas while the highest values where found for antenna pairs with around one quadrant inner antenna spacing.

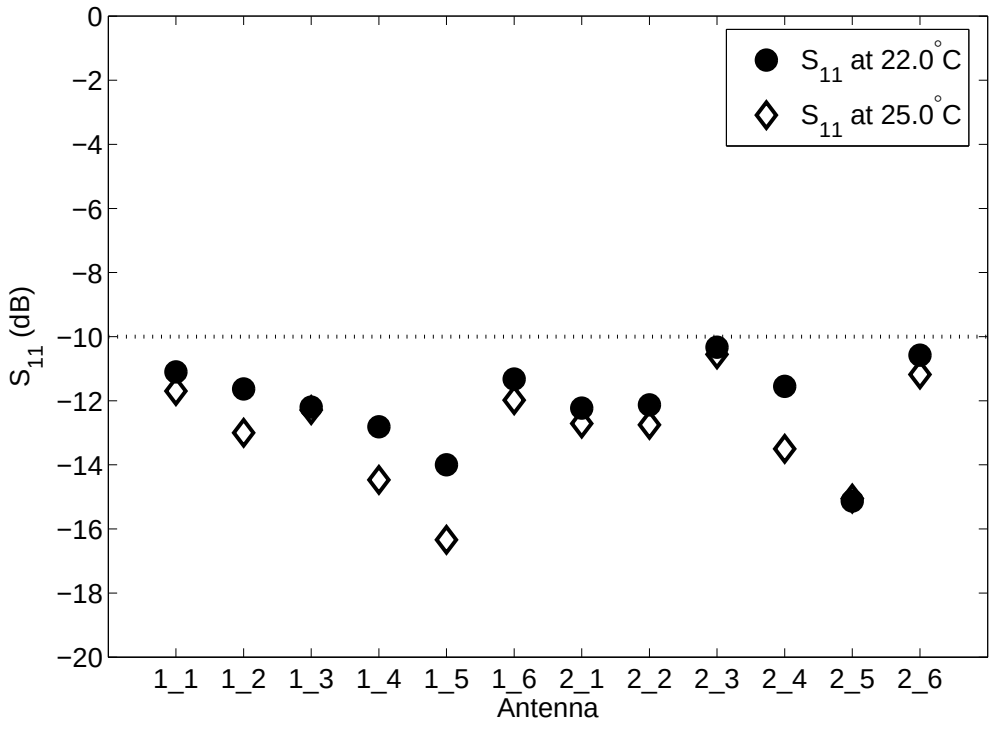

Figure 4: Reflection coefficients at 433.92MHz for each antenna of both arrays, e.g. 1_2 is the second antenna of the first antenna ring.

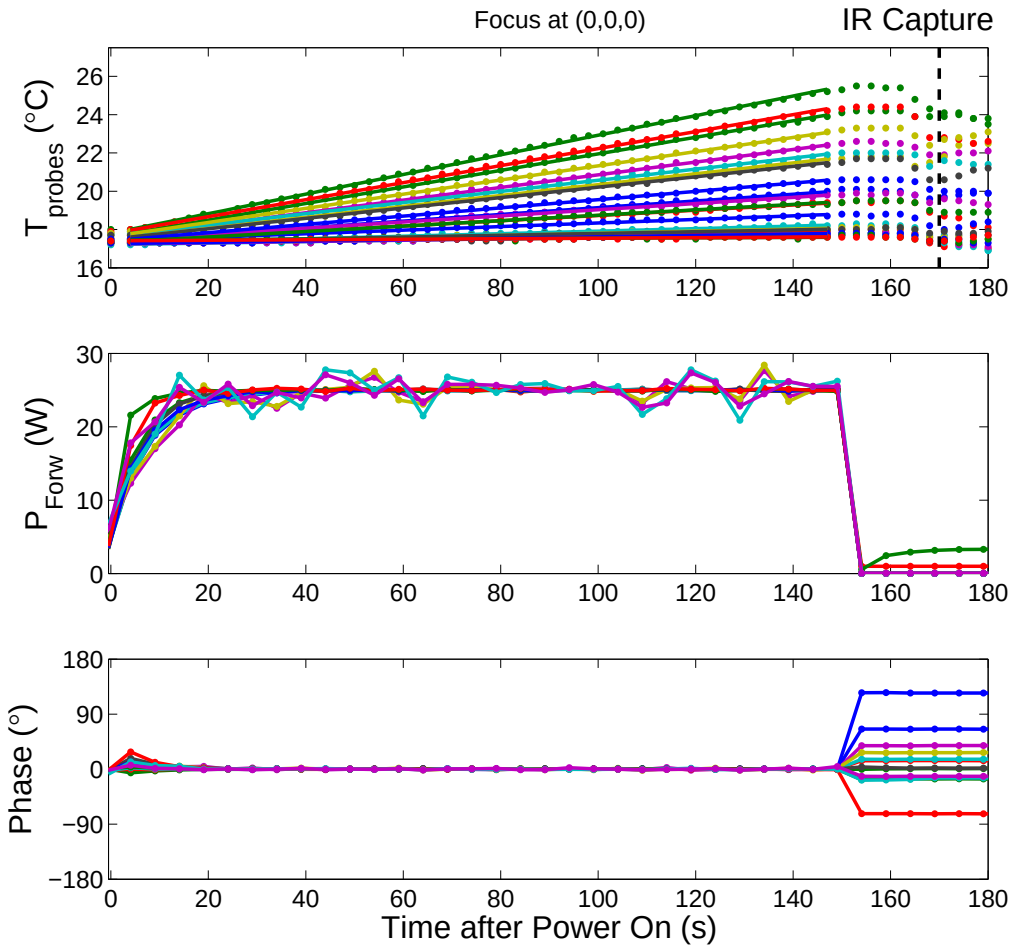

Figure 5: Temperature (T_{probes}) values and corresponding powers (P_{Forw}) and phases as function of time during an example powerpulse measurement. For the fiber probe temperature measurements (visualized in dots) we created linear fits (solid lines) and calculated the local SAR values from the slopes. IR pictures where captured before Power On and after Power Off (shown in the figure).

3.2 SAR tracks

Figure 5 visualizes an example of the measured temperatures with the fiber probes and the corresponding measured powers and phases. It shows the length of the power pulse and the corresponding temperature rise from which we calculated the local SAR values. In this example case, the upper halve of the prototype was removed approximately 160s after Power On and 10s later the IR picture was taken. The corrections by the control loop that are required to keep the power at the set value (25W) are clearly visible in the power curves. At start of the power pulse, the phases were influenced a little by the increase in power level, but these were automatically adjusted. The figure also shows that two amplifiers were leaking some power after power-off but this influence was relatively low (power-on: 300W vs power-off: ∼5W leakage). We found an almost perfect correlation between the measured temperatures and a linear fit, for all spatial locations ($r^2 = 1.0$), so we concluded that the influence of heat conductivity on the SAR measurements was negligible.

3.2.1 Comparison measurements and simulation

Figure 6 shows SAR values as function of the x-coordinate for TCP-based x-steering, i.e. for x = -30mm, x = 0mm and x = +30mm. Similarly, Figure 7 shows SAR values as function of the z-coordinate for TCP-based z-steering, i.e. for z = -50mm, z = -25mm and z = 0mm. For all IR thermography tracks we averaged over 10 pixels (one pixel was 0.7x0.7mm^2) to reduce noise. The tracks were normalized to their own maximum (IR thermography) or their own maximum of a spline-fit through the measurement points (T-probes and E-field sheet measurements). For central steering this maximum was typically around 0.6W/kg (normalized to 1W total input power). The desired focus point (TCP) is always indicated with the dashed line.

All measurements and predictions show that a central focus is obtained. As shown by these figures, this focus can be changed in radial (x) and axial (z) directions. Comparing the results of the three measurement methods we found a good qualitative agreement. Comparison of the simulations to these measurements reveals good agreement at central positions but discrepancies for more radial positions close to the PVC phantom border. The reason for this difference may lie in: 1) wrong dielectric properties of muscle phantom (lower conductivity) or 2) air-gaps at the connection between both halves of the setup. In the axial direction, there is an unexpected small asymmetry in the FDTD results for central settings (Figure 7a), this is probably caused by the asymmetry in the feeding of the antennas [17].

In radial direction, where the SAR patterns are most steep, the IR thermography curves show a somewhat flattened profile compared to the FDTD tracks. This flattening is caused

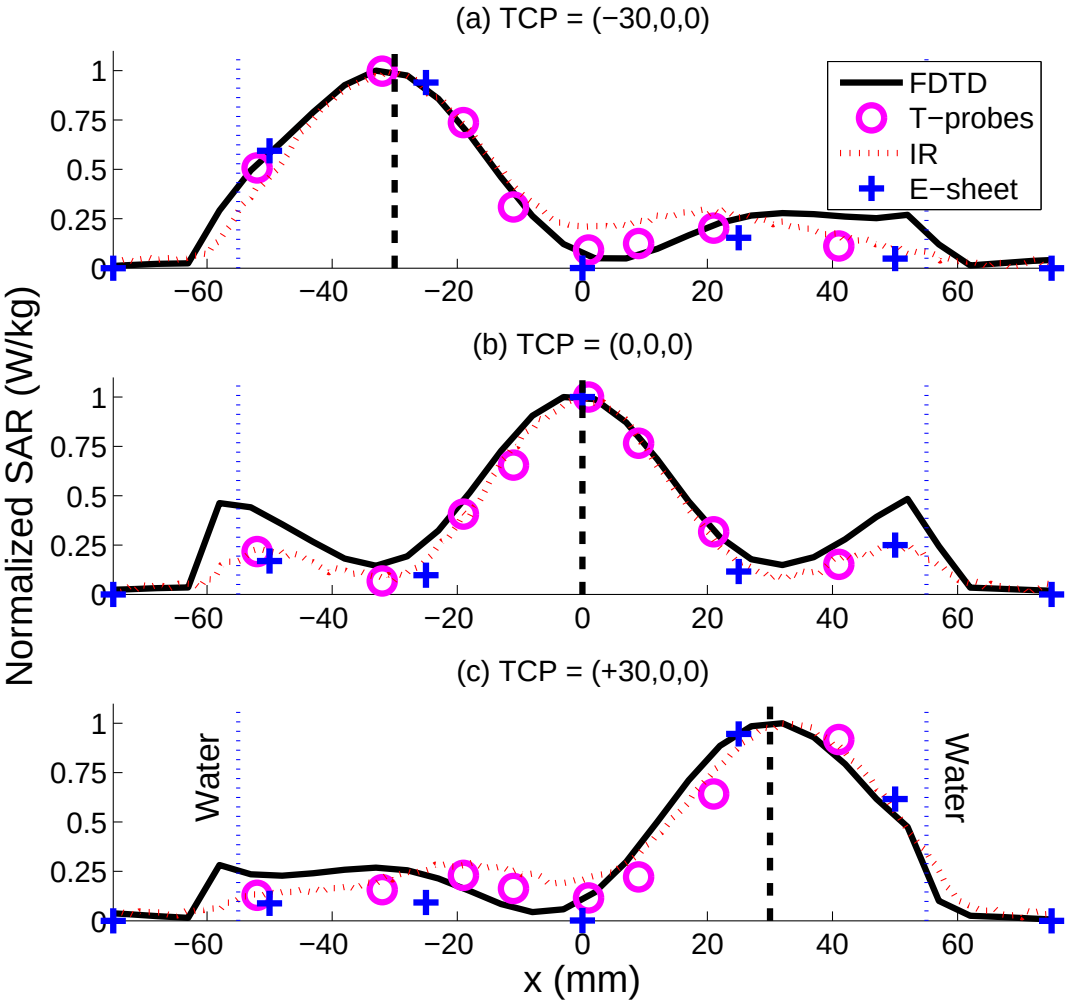

Figure 6: Simulated (FDTD) and measured (T-probes, IR and E-field sheet) SAR values at y = 0mm and z = 0mm for steering in the x-direction. All tracks are normalized to their own respective maximum value.

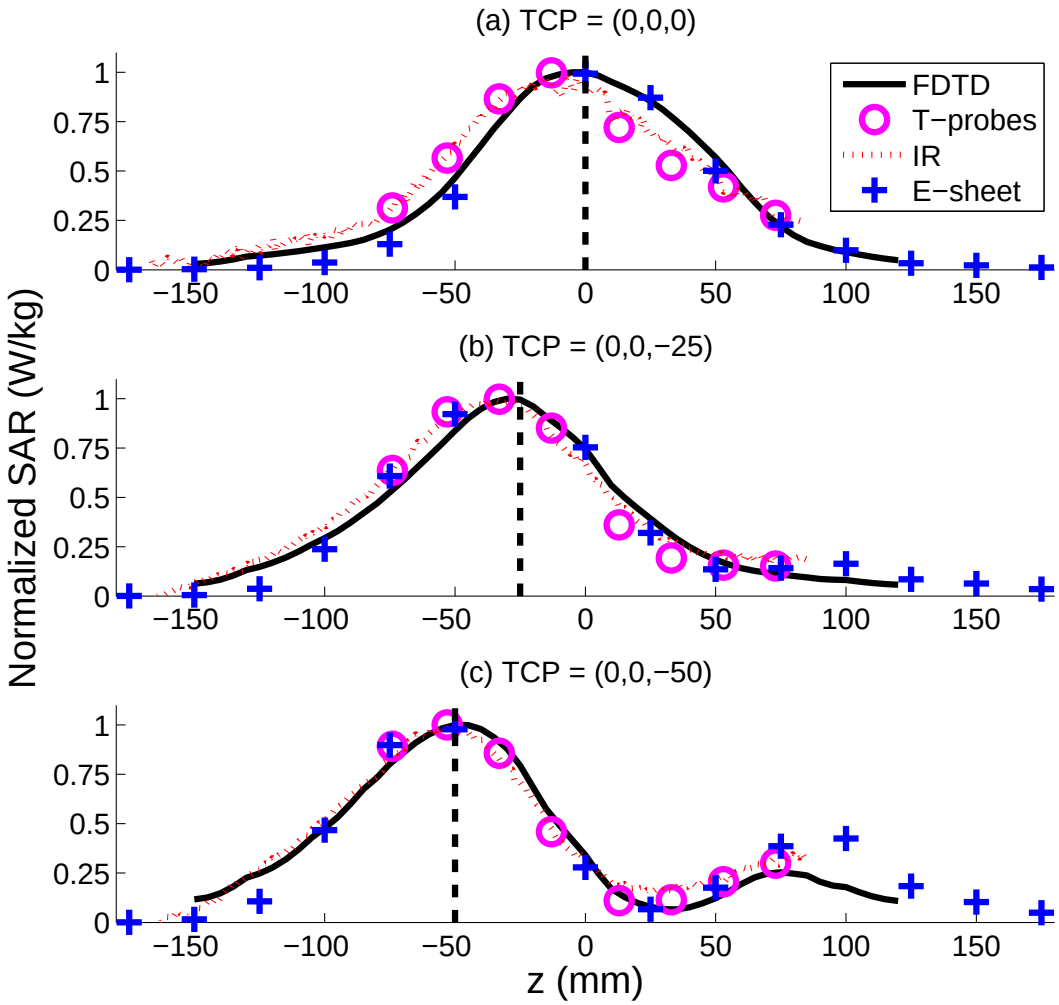

Figure 7: Simulated (FDTD) and measured (T-probes, IR and E-field sheet) SAR values at x = 0mm and y = 0mm for steering in the z-direction. All tracks are normalized to their own respective maximum value.

by thermal conduction during opening of the two halves after power application. After normalization this results in relatively higher values in the valleys of the curves because the maximum value is reduced. In axial direction this effect is less prominent because SAR curves are less steep. Further, the SAR values are decreased by the circulated water of the waterbolus of a stable temperature.

3.2.2 Determination of focus-size

Table 2: SAR steering (TCP setting (mm) and location of SAR_{max} (mm)) and corresponding focus-size (length $L_{50\%}$ (mm) and width $W_{50\%}$ (mm) of the 50% iso-SAR contour) parameters for the simulated (FDTD) and measured (IR thermography) tracks.

TCP setting	**Method**	**SAR**$_{max}$	$L_{50\%}$	$W_{50\%}$
Central	FDTD	(0,–,-1)	103	35
(0,0,0)	IR	(0,–,-5)	112 (+9%)	34 (-3%)
X-steering	FDTD	(31,–,0)	96	39
(+30,0,0)	IR	(32,–,0)	103 (+7%)	37 (-5%)
Z-steering	FDTD	(0,–,-50)	82	37
(0,0,-50)	IR	(0,–,-51)	87 (+6%)	38 (+3%)

Table 2 provides a summary of the most important parameters from Figure 6 and Figure 7. This table shows the SAR steering and corresponding focus-size parameters for the simulated (FDTD) and measured (IR thermography) tracks. The simulated SAR distribution for central settings and the focus-size parameters ($L_{50\%}$, $W_{50\%}$) are visualized in Figure 3. For the experimental verification of the predicted focus-size we used IR measurements due to its superior resolution and because its values correlated well with the T-probe measurements, which we assume to be more accurate. Table 2 shows that, using the TCP based phases, the obtained SAR focus can be steered towards the desired location with a reasonable accuracy, i.e. ∼5mm. Further, it indicates that the corresponding focus-lengths ($L_{50\%}$) are in the range of 87-112mm and the focus-widths $W_{50\%}$ are around 35mm.

3.3 Dynamic SAR steering

We used measurements with the E-field sheet to investigate the dynamic steering possibilities of the focus since no cooling down period is required for this method. We measured the location of maximum SAR and correlated this position to the TCP settings, which is visualized in Figure 8 (a,b). In this figure we show the maximum SAR location for x and z-steering along several tracks. These curves show a staircase shape due to the spatial resolution of the E-field sheet and because the use of a spline-fit to find the location of

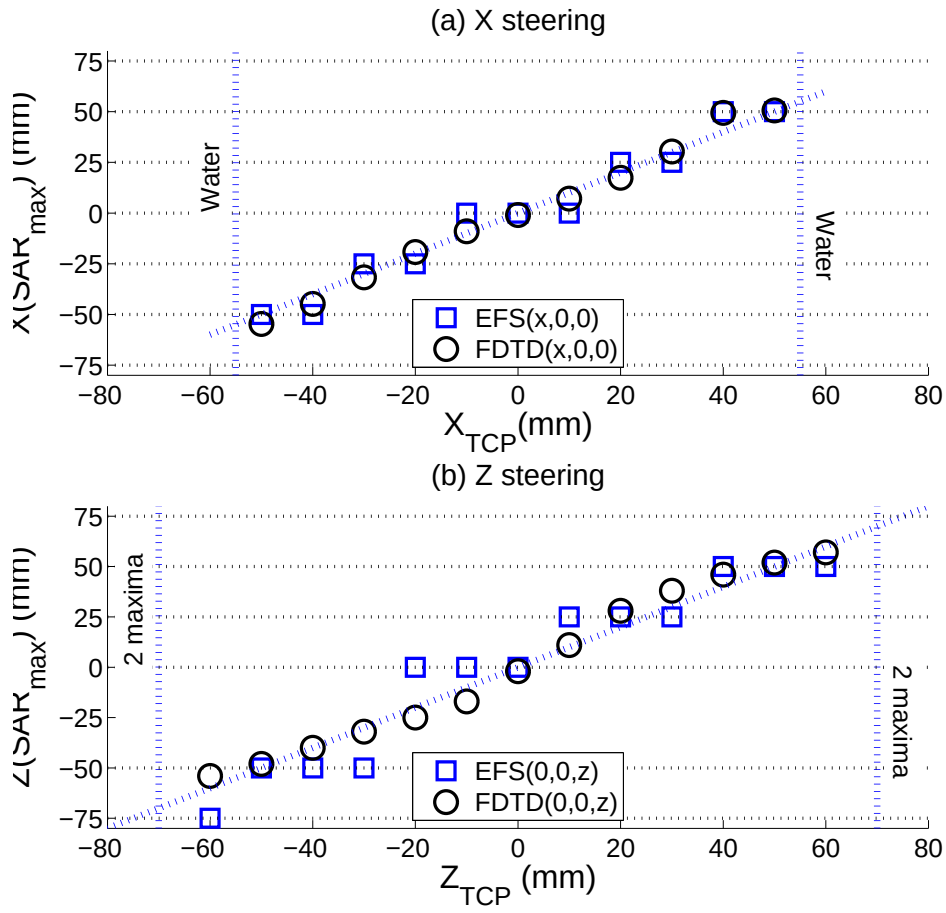

Figure 8: Measured maximum SAR point as function of TCP for SAR-steering in radial (a) and axial (b) directions. Locations of E-field sheet measurement points are indicated by the horizontal dotted lines and the unity curve by the diagonal dotted line. At z=-25mm there are no E-fields measured due to the design of the E-field sheets.

the maximum was omitted. We indicated the location of the E-field sheet diodes by the horizontal dotted lines and the identity curve, indicating a perfect match, by the vertical dotted line. Both figures show a linear relation and a high correlation between TCP location and location of maximum SAR, in both radial (x, and y due to symmetry) and axial (z) direction. This means that the focus can be accurately steered by using the TCP method to the desired location in the neck-equivalent muscle phantom. We further found that steering in the radial plane is possible in the entire phantom. In the z-direction, the focus can be steered till 60mm from the center. From this location a double focus distribution is obtained, i.e. the secondary focus becomes more than 50% of the maximum.

4 Discussion

4.1 Materials and methods

For this work we constructed a split-phantom setup consisting of two semi-cylinders that are closed with polymer sheets. In this way the setup provided the versatileness that enabled measurements between two parts with several measurement devices and IR measurements by opening the setup. The drawback of our approach is the possibility of air-gaps between the sheets which, especially for these high frequencies, can have a large effect on the local SAR and on the measurement accuracy. We have tried to decrease these influences by adding a little water between the sheets and some additional water pressure while the halves of the prototype are clamped together.

For the measurements we have used a muscle phantom recipe of Ito *et al.* [18]. Amounts of ingredients were used for muscle-equivalent properties ($\epsilon_r = 56$, $\sigma = 0.8$ S/m) at 22°C. These properties, however, vary with temperature and are very sensitive to small variations in salinity. Due to the required interference of multiple sources, these SAR values depend upon the conductivity in a non-linear fashion. By carrying out simulations with different conductivity values, we found that the SAR tracks in the x-direction are very dependent on conductivity, i.e. the lateral normalized SAR values are decreased by 30% for a 20% decrease in conductivity. Therefore, in future measurements we expect to improve the predictability of the measurements by measuring the properties of the phantom before each measurement.

4.2 Results

Electromagnetic models are used more and more for HT treatment planning and there is a growing use of EM models to perform parameters studies for the optimization of HT applicators [30] [31] [32]. While the accuracy of EM modelling has increased dramatically and high resolution simulations have become possible, up to now this has not led

to higher standards concerning model validations. Such a validation is a crucial step to assess dosimetry accuracy and will diminish the need for verification measurements for new applicators. For a superficial antenna, recently, a first attempt of such a quantitative validation by high resolution 3D measurements was presented by De Bruijne *et al.* [22]. This validation, however, was for a single antenna setup and should be confirmed for the SAR distributions with higher gradients that are normally obtained with array setups. For high accuracy SAR dosimetry validations of array setups, accurately on-site measured dielectric properties of all (phantom) materials are required. Further, an accurate measurement device is required, which in general is very expensive.

For our approach we used the availability of more accurate modeling for optimizing the entire HT applicator. To our knowledge, we were the first to use EM modeling to design an HT applicator from scratch by detailed parameter studies at frequencies above 400MHz. In a previous publication we have explained our work dedicated to the design of an optimized antenna positioning. Further, we used EM modeling to fully optimize the reflection characteristics of a single element of the antenna array. In the present paper we have experimentally verified the feasibility of focussed heating in the neck, which has been predicted earlier [12] [14], and as such to validate our approach. We further assessed the dimensions of the focus and verified the possibilities of dynamic steering. By comparing measurements to simulation we performed a qualitative verification of the predicted SAR patterns in a muscle phantom.

In this study we verified that a central focus can be obtained with a double ring of six antennas each. For central settings, we determined the width of this focus as 34mm (IR) and 35mm (FDTD) and the length as 112mm (IR) and 103mm (FDTD). This difference might be due to thermal conduction, which result in an overestimation of the EFS by IR thermography. In radial direction this size is normally $\lambda/3$ [27] [13], which means $\sim$31mm in a muscle phantom, and correlates well with the values in this study. In axial direction this focus is determined by a combined effect of the distance between the antenna rings, the radius of the antenna rings, and the operating frequency [14], i.e. the wavelength in muscle. The obtained focus can be steered in radial directions towards every point in the muscle phantom. In the axial direction (-z,z), extreme focus center point location is a 60mm off-center position.

For verification of the SAR profiles we used the split-phantom technique in combination with 1) glass-fiber thermometer probe measurements, 2) IR thermography using a high resolution IR camera, and 3) measurements using our Schottky diode E-field sheet. Local SAR values are determined for the first two (fiber-probes, IR) by using the power-pulse technique [33], i.e. high power is required, the latter (E-field) measurements were carried out at low power. The fiber-probe measurements have the advantage of a high accuracy and they provide the possibility to monitor temperatures during heating. Further, they are

non-metallic and very thin thus field-disturbances are negligible. The disadvantage of this method is the required cooling time after measurement (1-2hours) due to the high temperature gradients required. Further, multiple (multi-sensor) probes are required for a high resolution and positioning multiple probes in the split-phantom is cumbersome. IR thermography measurements with the most recent IR camera's have a high resolution which enables to investigate, besides the size of the focus, also the shape of the focus. IR measurements share the disadvantage of long cooling times. Further, for these measurements it is required to open up the setup to be able to take an IR picture, i.e. measurements were taken typically 10s after power off. According to Samaras *et al.* [24], for effective field size (EFS) measurements, this is sufficiently short for an accurate measurement. Although, compared to flat-phantom EFS measurements, the distributions obtained in this publication show much higher SAR gradients and therefore heat conduction might have somewhat more influence, by comparing the thermography results to the fiber probe measurement we could show that this influence remains low. By using the Schottky-diode E-field sheet [26] [25] we performed E-field measurements that can be performed at low power thus dynamic SAR steering with the prototype can be assessed. A major drawback of this equipment is its low resolution because it was designed for superficial hyperthermia applicator assessments in flat phantoms were the fields are more gradual. Further, in this split-phantom setup, air-gaps may be present which considerable decrease the sensitivity of the diodes. The superficial SAR values measurements by both power-pulse based methods further might have been hampered by the active water-cooling of the sides of the phantom. By the resemblance between the SAR derived from the E-field and temperature measurements, we conclude that this influence is low.

4.3 Quality assurance

Currently, no specific QA guidelines have been defined for our application or for newly developed applicators. Within the framework of ESHO, guidelines for ESHO protocols have been defined 1) for treatment of superficial tumours [33], i.e. locally advanced breast carcinoma, advanced neck nodes, malignant melanoma, and 2) for regional hyperthermia in the pelvic area by radiofrequency equipment [34]. In terms of (regular) assessment of the SAR pattern of an applicator, clearly different approaches are suggested. For superficial QA guidelines and assessment of applicator performance, the effective field size (EFS) and penetration depth (PD) are defined, which "should be determined by measuring the -changes in temperature resulting from a brief pulse of high power" [33]. In these guidelines, the necessity for an additional characterization of the SAR pattern corresponding to a multi-element array of applicators is recognized. Further, it is mentioned that if "non-perturbing E-field probes, thermographic imaging or liquid-crystal sheet imaging" are used, they should be corroborated by measurements obtained using the power pulse

technique. A requirement for using this technique is that 60s after power-on the EFS and PD should be determined. However, by finding perfect linear temperature curves, we showed that longer heating periods can be used. In the guidelines for regional hyperthermia [34], it is required for SAR distribution characterization of equipment to perform system performance regularly using the LED matrix/lamp phantom using different phase/amplitude settings, different phantom positions and different bolus configurations. The E-field Schottky-diode sheet system is compliant to all requirements but a higher resolution is required so the focus size and shape can be determined as well, i.e. $\sim \lambda/10$ in stead of $\sim \lambda/4$ (at 433MHz). Further, to obtain a more homogeneous temperature distribution, an improvement would be to use a liquid phantom material. The required new E-field sheet system, however, must be specifically designed and other questions remain to be solved.

5 Conclusions

In this paper we analyzed the ability of using a phased array hyperthermia applicator for focussed heating in the head and neck region. Firstly, we conclude that the early design of the patch antenna, in a well controlled water environment, provides an average efficiency of 94%, which is highly sufficient for our investigations. Further, we measured low cross-coupling between antennas in the array (maximum -22dB). Thirdly, we conclude that, using the analyzed setup of two rings of six antennas, focussed heating in the head and neck is feasible. By IR thermography we measured a central 50% iso-SAR focus of 112mm in axial and 34mm in radial direction in a muscle phantom. This radial dimension is sufficiently small to allow targeted heating of advanced tumours and by de-focussing also good SAR coverage of larger tumours should be possible. The axial length of this focus is somewhat large for tumour-specific heating, however this results in blood pre-heating because vessels are mainly oriented in this direction. The focus can be steered in direction to maximum 60cm from the center in the phantom. Combined with the focus size of 10cm in axial direction, this indicates that 50% SAR coverage may be possible up to 11cm from a central location. The actual extend of heating in a patient remains to be determined.

We found little differences between the predictions of the SAR distribution by the three investigated measurement methods. Therefore, as best system for regular quality assurance we chose the Schottky-diode E-field sheet system. This device enables quick measurements and better control of the temperatures resulting in more predictable dielectric properties of the phantom materials. However, a modified design of the Schottky-diode E-field sheet system is required that provides a higher resolution and better reduction possibilities of air-gaps.

6 Acknowledgements

This work is supported by the Maurits and Anna de Kock foundation and the Dutch Cancer Society, grant DDHK 2003-2855. We further would like to thank the workshop of the department of Radiation Oncology for the construction of the prototype and T.A. ter Meer, H. Schippers and W. Schaap of the Dutch Aerospace Laboratory (NLR) for their work on the signal measurement equipment. And lastly, we thank H. Strijbos and A.P.M. Zwamborn of TNO (The Hague) for their contributions to the discussions.

References

[1] El-Sayed S, Nelson N. Adjuvant and adjunctive chemotherapy in the management of squamous cell carcinoma of the head and neck region: a meta-analysis of prospective and randomized trials. *J Clin Oncol* 1996; 14: 838-847.

[2] Pignon JP, Bourhis J, Domenge C, et al. Chemotherapy added to locoregional treatment for head and neck squamous-cel carcinoma: three meta-analyses of updated individual data. *Lancet* 2000; 355: 949-955

[3] Trotti A. Toxicity in head and neck cancer: a review of trends and issues. *Int J Radiat Oncol Biol Phys* 2000; 47: 1-12.

[4] Huilgol NG. A phase I study to study arsenic trioxide with radiation and hyperthermia in advanced head and neck cancer. *Int J Hyperthermia* 2006; 22: 391-397.

[5] van der Zee J, Gonzalez Gonzalez D, van Rhoon GC, et al. Comparison of radiotherapy alone with radiotherapy plus hyperthermia in locally advanced pelvic tumours: a prospective, randomised, multicentre trial. Dutch Deep Hyperthermia Group. *Lancet* 2000; 355: 1119-1125.

[6] Colombo R, Da Pozzo LF, Salonia A, et al. Multicentric study comparing intravesical chemotherapy alone and with local microwave hyperthermia for prophylaxis of recurrence of superficial transitional cell carcinoma. *J Clin Oncol* 2003; 21: 4270-4276.

[7] Jones E, Thrall D, Dewhirst MW, et al. Prospective thermal dosimetry: the key to hyperthermia's future. *Int J Hyperthermia* 2006; 22: 247-253.

[8] Valdagni R, Liu F-F, Kapp S. Important prognostic factors influencing outcome of combined radiation and hyperthermia. *Int J Radiat Oncol Biol Phys* 1988; 15: 959-972.

[9] Valdagni R, Amichetti M. Report of long-term follow-up in a randomized trial comparing radiation therapy and radiation therapy plus hyperthermia to metastatic lymphnodes in stage IV head and neck patients. *Int J Radiat Oncol Biol Phys* 1993; 28: 163-169.

[10] Wust P, Seebass M, Nadobny J, et al. Simulation studies promote technological development of radiofrequency phased array hyperthermia. *Int J Hyperthermia* 1996; 12: 477-494.

[11] Stauffer PR. Evolving technology for thermal therapy of cancer. *Int J Hyperthermia* 2005; 21: 731744.

[12] Paulides MM, Vossen SHJA, Zwamborn APM, et al. Theoretical investigation into the feasibility to deposit RF energy centrally in the head and neck region. *Int J Radiat Oncol Biol Phys* 2005; 63: 634-642.

[13] Paulides MM, Wielheesen DHM, van der Zee J, et al. Assessment of the local SAR distortion by major anatomical structures in a cylindrical neck phantom. *Int J Hyperthermia* 2005; 21: 125-140.

[14] Paulides MM, Bakker JF, Zwamborn APM, et al. A head and neck hyperthermia applicator: theoretical antenna array design. *Int J Hyperthermia* In press.

[15] Seebass M, Beck R, Gellerman J, et al. Electromagnetic phased arrays for regional hyperthermia: optimal frequency and antenna arrangement. *Int J Hyperthermia* 2001; 17: 321-336.

[16] Paulsen KD, Geimer S, Tang J, et al. Optimisation of pelvic heating rate distributions with electromagnetic phased arrays. *Int J Hyperthermia* 1999; 15: 157-186.

[17] Paulides MM, Bakker JF, Chavannes N et al. A patch antenna design for a phased-array head and neck hyperthermia applicator. *IEEE Trans. Biom. Eng.* Submitted for publication.

[18] Ito K, Furuya K, Okano Y, et al. Development and Characteristics of a Biological Tissue-Equivalent Phantom for Microwaves. *Electronics and Communications in Japan* 2001; 84; 67-77

[19] Gabriel S, Lau RW, Gabriel C. The dielectric properties of biological tissues III: Parametric models for the dielectric spectrum of tissues. *Phys Med Biol* 1996; 41: 2271-2293.

[20] SEMCAD: the Simulation platform for EMC, Antenna Design and Dosimetry
Smith and Partner Engineering AG
http://www.semcad.com

[21] Samaras T, Rietveld PJM, van Rhoon GC. Effectiveness of FDTD in Predicting SAR Distributions from the Lucite Cone Applicator. *IEEE Trans Micr Theor Tech* 2000; 48: 2059-2063

[22] de Bruijne M, Samaras T, Neufeld E, et al. Quantitative three-dimensional SAR validation of the Lucite cone applicator. abstracts of 22nd Annual Meeting of the ESHO, Graz, Austria, June 2005

[23] Stogryn A. Equations for Calculating the Dielectric Constant of Saline Water (Correspondence). *IEEE Trans Micr Theor Tech* 1971; 19: 733-736.

[24] Samaras T, van Rhoon GC, Sahalos JN. Theoretical investigation of measurement procedures for the quality assurance of superficial hyperthermia applicators. *Int J Hyperthermia* 2002; 18: 416-425.

[25] Kaatee RSJP, van Rhoon GC. An electric field measurement system, using a two-dimensional array of diodes. *Int J Hyperthermia* 1999; 15: 441-454.

[26] van Rhoon GC, Ameziane A, Lee WM, et al. Accuracy of electrical field measurement using the flexible Schottky diode sheet at 433 MHz. *Int J Hyperthermia* 2003; 19: 134-144.

[27] Van Rhoon GC, Van Der Heuvel DJ, Ameziane A, et al. Characterization of the SAR-distribution of the Sigma-60 applicator for regional hyperthermia using a Schottky diode sheet. *Int J Hyperthermia* 2003; 19: 642-654.

[28] Sigma eye applicator operator manual. BSD Medical Corporation, 1995.

[29] Turner PF, Schaeffermeyer T. BSD-2000 approach for deep local and regional hyperthermia. *Strahlentherapie und Oncologie* 1989; 165: 738-741.

[30] Kroeze H, Van de Kamer JB, De Leeuw AA, et al. Regional hyperthermia applicator design using FDTD modelling. *Phys Med Biol* 2001; 46: 1919-1935.

[31] Nadobny J, Wlodarczyk W, Westhoff L, et al. Development and evaluation of a three-dimensional hyperthermia applicator with Water-COated Antennas (WACOA). *IEEE Med Phys* 2003; 30: 2052-2064.

[32] Siauve N, Nicolas L, Vollaire C, et al. Optimization of the sources in local hyperthermia using a combined finite element-genetic algorithm method. *Int J Hyperthermia* 2004; 20: 815-833.

[33] Hand JW, Lagendijk JJW, Bach Andersen J, et al. Quality assurance guidelines for ESHO protocols. *Int J Hyperthermia* 1989; 5: 421-428.

[34] Lagendijk JJW, van Rhoon GC, Hornsleth SN, et al. ESHO quality assurance guidelines for regional hyperthermia. *Int J Hyperthermia* 1998; 14: 125-133.